

1 **Forecasting Carbon Monoxide on a Global Scale for the** 2 **ATom-1 Aircraft Mission: Insights from Airborne and** 3 **Satellite Observations and Modeling**

4
5 Sarah A. Strode^{1,2}, Junhua Liu^{1,2}, Leslie Lait^{2,3}, Róisín Commane⁴, Bruce Daube⁴, Steven Wofsy⁴, Austin
6 Conaty^{2,5}, Paul Newman², Michael Prather⁶

7
8 ¹Universities Space Research Association, Columbia, MD, USA

9 ²NASA GSFC, Greenbelt, MD, USA

10 ³Morgan State University, Baltimore, MD, USA

11 ⁴Harvard University, Cambridge, MA, USA

12 ⁵SSAI, Greenbelt, MD, USA

13 ⁶University of California, Irvine, CA, USA

14
15 *Correspondence to:* Sarah A. Strode (sarah.a.strode@nasa.gov)

16
17 **Abstract** The first phase of the Atmospheric Tomography Mission (ATom-1) took place in July-August of
18 2016 and included flights above the remote Pacific and Atlantic oceans. Sampling of atmospheric
19 constituents during these flights is designed to provide new insights into the chemical reactivity and processes
20 of the remote atmosphere and how these processes are affected by anthropogenic emissions. Model
21 simulations provide a valuable tool for interpreting these measurements and understanding the origin of the
22 observed trace gases and aerosols, so it is important to quantify model performance. GEOS-5 forecasts and
23 analyses show considerable skill in predicting and simulating the CO distribution and the timing of CO
24 enhancements observed during the ATom-1 aircraft mission. We use GEOS-5's tagged tracers for CO to
25 assess the contribution of different emission sources to the regions sampled by ATom-1 to elucidate the
26 dominant anthropogenic influences on different parts of the remote atmosphere. We find a dominant
27 contribution from non-biomass burning sources along the ATom transects except over the tropical Atlantic,
28 where African biomass burning makes a large contribution to the CO concentration. One of the goals of
29 ATom is to provide a chemical climatology over the oceans, so it is important to consider whether August
30 2016 was representative of typical boreal summer conditions. Using satellite observations of 700 hPa and
31 column CO from the Measurement of Pollution in the Troposphere (MOPITT) instrument, 215 hPa CO from

32 the Microwave Limb Sounder (MLS), and aerosol optical thickness from the Moderate Resolution Imaging
33 Spectroradiometer (MODIS), we find that CO concentrations and aerosol optical thickness in Aug. 2016
34 were within the observed range of the satellite observations, but below the decadal median for many of the
35 regions sampled. This suggests that the ATom-1 measurements may represent relatively clean but not
36 exceptional conditions for lower tropospheric CO.

37 **1 Introduction**

38 The first phase of the NASA Atmospheric Tomography Mission (ATom-1)
39 (<https://espo.nasa.gov/atom>) took place in July-August 2016. The aircraft completed a circuit beginning in
40 Palmdale, California and traversing the remote Pacific and Atlantic oceans, providing an unprecedented
41 picture of the chemical environment at a wide range of latitudes over the remote oceans. Major goals of the
42 Atom mission include identifying chemical processes that control the concentrations of short-lived climate
43 forcers, quantifying how anthropogenic emissions affect chemical reactivity globally, and identifying ways
44 to improve the modeling of these processes,

45 Chemical forecasts from the GEOS-5 model provided insight into the chemical environments and
46 sources of pollution for the diverse regions sampled during the ATom-1 campaign. GEOS-5 forecasts help
47 determine the source regions and emission types that contribute to the trace gas and aerosol concentrations
48 measured during ATom, which is directly relevant to the goal of quantifying how anthropogenic emissions
49 affect global chemical reactivity. GEOS-5 supports numerous aircraft missions, and validation of the model
50 forecasts is important for developing confidence in and understanding the limitations of chemistry forecasting
51 for aircraft missions. The ATom dataset, which uses unbiased sampling rather than chasing plumes, provides
52 a unique opportunity to validate the overall performance of the GEOS-5 model on a global scale.

53 One of the goals of ATom is to provide an observation-based climatology of important atmospheric
54 constituents and their reactivity in the remote atmosphere. Consequently, it is important to examine whether
55 the ATom observations are temporally and spatially representative of the broader remote atmosphere.
56 *Prather et al.* (2017) examined the ability of observations from a single path to represent the variability of a
57 broader geographic region, but noted that year-to-year and El Niño/Southern Oscillation (ENSO) variability
58 could also be important. Year to year variability in meteorology and emissions both contribute to interannual
59 variability in trace gases and aerosols, so it is important to consider the temporal representativeness of a
60 single season sampled by ATom. For example, ENSO is a major driver of variability in ozone distributions
61 (*Ziemke and Chandra*, 2003), and large biomass burning events during El Niño years increase concentrations
62 of trace gases including CO and CO₂ (*Langenfelds et al.*, 2002). Biomass burning plays a particularly strong
63 role in driving the interannual variability of CO (e.g. *Novelli et al.*, 2003; *Kasischke et al.*, 2005; *Duncan and*
64 *Logan*, 2008; *Strode and Pawson*, 2013; *Voulgarakis et al.*, 2015;). The impacts of large biomass burning
65 events during El Niño events are visible in satellite observations of CO (e.g. *Edwards et al.*, 2004; *Edwards*
66 *et al.*, 2006; *Logan et al.*, 2008, *Liu et al.*, 2013). *Pfister et al.* (2010) used a chemistry transport model (CTM)
67 as well as satellite data to examine the CO sources and transport over the Pacific during the INTEX-B mission

68 compared to previous years. They found biomass burning to be the largest contributor to interannual
69 variability, despite its lower emissions compared to fossil fuel sources. Here we show how the time and place
70 of ATom-1 measurements fit into a global, multi-year climatology of CO. In particular, we assess the extent
71 to which measurements from the ATom-1 period represent the CO and aerosol distributions over the last
72 decade and a half.

73 In this study, we place the August 2016 ATom observations in the context of interannual variability and
74 assess the contributions of different emission sources to the various regions sampled during the campaign.
75 We focus on CO, a tracer of incomplete combustion whose lifetime of 1-2 months allows long-range transport
76 to the remote oceans. Section 2 describes the model and observations used in this analysis. Section 3
77 compares the GEOS-5 CO to observations. Section 4 discusses the global distribution of CO, and presents
78 the relative CO source contributions to the regions sampled by ATom. Section 5 presents an analysis of the
79 interannual variability in CO and aerosol optical thickness seen in satellite observations to assess how well
80 August 2016 observations represent climatological August conditions. Section 6 summarizes our
81 conclusions.

82 **2 Observations and Model**

83 **2.1 ATom Observations**

84 ATom-1 flew transects through the Pacific, Southern, Atlantic and Arctic oceans with the NASA DC8
85 aircraft in August 2016. Each of the 11 flights included sampling from the boundary layer to the top of the
86 aircraft range (39 kft). We use the ATom-1 data (July-August 2016) [*Atom Science Team, 2017*] for
87 comparison with the model forecasts and analyses.

88 We take ATom-1 CO observations from the Harvard QCLS instrument (*Santoni et al., 2014*), which
89 has a history of successful measurements during the HIAPER Pole-to-Pole Observations (HIPPO) campaign.
90 Briefly, the instrument uses a pulsed quantum cascade laser at 2160 cm^{-1} to measure absorption of CO through
91 a astigmatic multi-pass sample cell (with 76 m path length), with detection using liquid nitrogen cooled
92 HgCdTe detector. A separate laser and detector are used to measure methane and nitrous oxide in the same
93 cell. Inflight calibrations were conducted with gases traceable to the NOAA WMO (X2014) scale, with
94 calibration of tanks before ATom1 and after ATom2 (February 2017) showing no significant change in the
95 CO concentration in the gas standards. The inlet for the instrument was specially designed for the DC-8
96 aircraft. The QCLS observations have an accuracy and precision of 3.5 ppb and 0.15 ppb, respectively. The
97 QCLS observations used in this analysis are being archived at the ORNL DAAC
98 (<https://doi.org/10.3334/ORNLDAAC/1604>).

99

100 2.2 Satellite Observations

101 We use satellite observations that cover more than a decade to examine the interannual variability
102 of CO and aerosols. We focus on satellite observations because they provide broad coverage over the oceans,
103 where surface data is sparse. The Measurement of Pollution in the Troposphere (MOPITT) instrument, which
104 flies on the Terra satellite, provides CO observations beginning in 2000 (*Edwards et al.*, 2004). We use the
105 version 6 thermal infrared (TIR) level 3 product (*Deeter et al.*, 2014). The MOPITT TIR averaging kernels
106 show high sensitivity to CO between 700 and 500 hPa (*Emmons et al.*, 2007). We use the CO column and
107 700 hPa CO retrievals.

108 The Microwave Limb Sounder (MLS) (*Waters et al.*, 2006), which flies on the Aura satellite,
109 provides useful observations of CO down to 215 hPa (*Livesey et al.*, 2008) beginning in 2004. We use the
110 Version 4.2 level 2 data for the 215 hPa level with the recommended quality, status, precision, and
111 convergence criteria. Although MLS data overlap with ATom only at the highest flight levels, both it and
112 MOPITT provide complementary views of CO in the lower troposphere and upper troposphere/lower
113 stratosphere (UTLS), respectively. The MOPITT averaging kernels include some sensitivity to the 200 hPa
114 level, implying a small overlap between the MOPITT and MLS observations.

115 The Moderate Resolution Imaging Spectroradiometer (MODIS) instrument on the Aqua satellite
116 provides column aerosol optical thickness (AOT) data beginning in 2002. We use MODIS data in this
117 analysis because it provides a relatively long data record. We use the Collection-6 level 2 (MYD04_L2)
118 [*Levy et al.*, 2015] 550 nm AOT data over oceans aggregated into 0.5 degree grid boxes, and then take
119 monthly means with the daily data weighted according to the QA.

120 2.3 Model Description

121 We use chemical forecasts and analyses from the GEOS-5 Forward Processing (FP) system to
122 quantify the contribution of different emission sources to the observed CO distribution and to identify the
123 origin of observed plumes. A global model is necessary for this analysis since CO is transported globally.
124 The FP stream from the Global Modeling and Assimilation Office (GMAO) generates GEOS-5 forecast
125 products as well as assimilation products using the most current system approved for near-real-time
126 production. We use the FP system in our study because it is the system used to generate forecasts that are
127 used during ATom and other aircraft missions, and is thus relevant to future mission and flight planning. The
128 GEOS-5 model (*Molod et al.*, 2015) is a global general circulation model (GCM) with 72 vertical levels
129 reaching from the surface to 1 Pa. The assimilation system is described in (*Rienecker et al.*, 2008; *Rienecker*
130 *et al.*, 2011), and includes assimilation of ozone measurements from the Ozone Monitoring Instrument (OMI)
131 and MLS, and aerosol optical depth as well as meteorological variables. The forward processing system
132 produces output on 72 model levels or 42 pressure levels with 5/16 by 1/4 degree horizontal resolution. Our
133 study uses the pressure level output.

134 The GEOS-5 FP system (*Lucchesi*, 2017) simulates the transport of CO as well as tagged CO tracers
135 from specific regions and sources, which helps track the transport of pollution outflow. Tagged tracers are

136 available for biomass burning (BB) globally as well as biomass burning from Eurasia, North America, Africa,
137 and Central and South America; and for non-BB sources globally and from Europe, Asia, and North America.
138 Non-BB sources include fossil fuels, biofuels, CO from oxidation of biogenic VOCs, and CO from methane
139 oxidation, as described in *Ott et al.* (2010). Supplemental Figure S1 shows the regions included in each
140 tagged tracer. *Bian et al.* (2013) used observations of dichloromethane and acetonitrile from the ARCTAS
141 mission to validate the anthropogenic and biomass burning CO tracers, respectively.

142 Daily-varying biomass burning emissions come from the Quick Fire Emission Dataset (QFED)
143 version 2 [*Darmenov and da Silva*, 2015], which is based on fire radiative power from the MODIS
144 instrument. Thus the BB emissions include day-to-day and interannual variability, but the non-BB sources
145 and the OH fields use monthly means and lack daily-scale variability and interannual variability. Table 1
146 presents the August emission inputs for the major regions considered. CO emissions are then scaled up by
147 20% for fossil fuels and 11% for biomass burning to account for CO production from co-emitted VOCs, since
148 VOC's are not explicitly carried in the GEOS-fp chemical mechanism. This approach was developed by
149 *Duncan et al.* (2007) to account for the CO source from non-methane hydrocarbon oxidation.

150 CO from methane oxidation is included in the non-BB tagged tracers for the regions in which
151 oxidation occurred. For example, if methane is oxidized over North America, the resulting CO is included
152 in the North American non-BB tracer. The monthly mean methane fields come from a GMI Chemistry and
153 Transport Model (CTM) simulation, which uses prescribed zonal mean surface concentrations. CO is lost
154 by reaction with OH using fixed monthly OH fields archived from the GMI CTM. Supplemental Figure S2
155 shows the methane and OH fields included in the FP system.

156 **3 GEOS-5 Chemical Forecasting for ATom**

157 During the ATom mission, the GEOS-5 model is engaged to provide chemical forecasts for each flight
158 that include the major chemical species and, for CO, tagged tracers for different sources. The chemical
159 forecasts are used together with meteorological forecasts for day-to-day flight planning, although flight tracks
160 were intentionally not altered to chase specific chemical features to avoid a highly biased sampling of
161 pollution. The chemical forecasts provide the ATom team with a preview of the chemical environments that
162 the flight is expected to sample, including the location of pollution, biomass burning, or dust plumes; regions
163 of substantial but well-mixed anthropogenic pollution; and cleaner regions. The forecasts also provide a
164 broader spatial context for the observations, since the 3-dimensional model output shows the spatial extent
165 of features that intersect the flight track.

166 We examine the performance of the GEOS-5 forecasts by comparing the simulated CO to the QCLS
167 observations. The forecasts provided during the mission used forecast wind fields, with the forecast lead
168 time varying depending on the timing of the flight. For consistency, the results shown here use the CO
169 simulated with the assimilated wind fields, but we note that similar features were seen for the CO simulated
170 with the forecast winds, as further discussed in section 3.1.2. For the model results, we do not apply temporal
171 interpolation between the model output frequency (6 hours). Instead, we sample the model forecasts at the

172 time closest to the mid-point of each flight segment. To compare with observations, the 3D model forecast
173 was interpolated to the longitude, latitude and pressure given in the 10-second merges of the ATom
174 measurements.

175 **3.1 Analysis of CO along the Meridional Flight Tracks**

176 We compare CO from GEOS-5 to the QCLS CO observations for specific flights, using the 10-
177 second merge files. The GEOS-5 CO is taken from the 3D field at the time closest to the mid-point of the
178 flight and interpolated in space to the flight track. The ATom flight tracks are shown in Supplemental Figure
179 S3. We focus on two sections of the ATom-1 circuit: the North to South flights through the Pacific, and the
180 South to North flights through the Atlantic, although we briefly discuss the other flights as well. These two
181 transects allow us to examine the transition from northern hemispheric to tropical to southern hemispheric
182 influence.

183 **3.1.1 Pacific legs**

184 Figure 1 shows CO from the three Pacific flights spanning Anchorage, Alaska to Christchurch, New
185 Zealand. The top panels show the GEOS-5 curtain of CO along the flight track, with the QCLS observations
186 overplotted in circles. The observations show higher values of CO in the first half of the Anchorage-Kona
187 flight compared to the other portions of the Pacific, and this feature is reproduced in GEOS-5 as well. GEOS-
188 5 agrees well with the observed mean value for CO on this flight (Table 2). Tagged tracers (Fig. 1 bottom
189 panels) show that non-BB sources, especially from Asia, are the dominant contributor to CO levels
190 throughout the Pacific, and the decrease in Asian non-BB CO explains the observed decrease in CO as the
191 flights move south.

192 The observations show plumes of enhanced CO scattered throughout all three Pacific flights,
193 although they are most intense in the north Pacific, as seen in the Anchorage-Kona flight. GEOS-5 typically
194 reproduces the timing of these plumes, but the magnitude is usually underestimated, particularly for the
195 strongest plumes. This leads to an underestimate of the observed standard deviation of the CO on the
196 Palmdale-Anchorage (Fig. S4) and Anchorage-Kona flights (Table 2). In addition to biases in emissions,
197 observations often show fine-scale structures too small for the model to resolve (Hsu et al., 2004), and
198 underestimating the concentrations in strong plumes is a common problem for global models (e.g. *Heald et*
199 *al.*, 2003). Either biases in emissions or insufficient vertical or horizontal model resolution may thus be
200 responsible for the underestimate. The tagged tracer for biomass burning shows a small increase at the time
201 of the underestimated plumes near hour 22 of the Anchorage-Kona flight (Fig. 1d,g), suggesting that those
202 underestimates are due to the insufficient magnitude of the simulated biomass burning plumes. An exception
203 is in the tropical Pacific (Kona-Pago Pago flight), in which GEOS-5 predicted some enhancements, driven
204 by fossil fuels, not seen in the observations. Tagged tracers indicate that Asian non-BB CO drove many of
205 the observed enhancements, while others were due to biomass burning.

206 In the south Pacific (Pago Pago to Christchurch segment), the flight sampled the stratosphere three
207 times, with CO levels decreasing to approximately 30 ppb, as shown in Fig. 1c. As expected from

208 stratospheric chemistry and seen in previous observations, both ATom-1 and GEOS-5 show a strong decrease
209 in CO as the flight rises above the tropopause, with GEOS-5 underestimating the observed gradient. Both
210 the model and measurements show tropospheric CO less than 90 ppbv along the flight route with slightly
211 elevated CO above 600 hPa around T22:00 and T24:00. For this flight and the subsequent flight to Punta
212 Arenas, all observations are in the Southern Hemisphere and the mean values for both ATom-1 and GEOS-
213 5 agree within the range 54-57 ppb (Table 2, Fig S5).

214 3.1.2 Atlantic Legs

215 The ATom flights traversed the Atlantic from South to North, beginning in Punta Arenas, Chile and
216 ending in Kangerlussuaq, Greenland. Figure 2 shows the Atlantic flights from Punta Arenas to Ascension
217 Island to the Azores to Kangerlussuaq. GEOS-5 has an excellent simulation of background CO values seen
218 on these flights, with the mean values falling within 2 ppb of the observations (Table 2) while the mean
219 observed values for each flight shift from 69 to 101 to 88 ppb. The observations show plumes of high CO
220 intersecting the flight track on all three flights. GEOS-5 also shows plumes of enhanced CO at these
221 locations, but the magnitude is often underestimated (Fig. 2d-f), especially for the Azores-Kangerlussuaq
222 flight. Supplemental Figure S6 shows the CO results for the Azores-Kangerlussuaq flight using forecast
223 wind fields, and illustrates the temporal evolution of CO plumes along the flight track. Comparison of Fig.
224 S6 with Fig. 2f shows that the impact of using analysis versus forecast wind fields is small for this flight
225 since the forecasts already capture the timing of the plumes.

226 Non-BB sources dominate the background CO levels on all three flights. However, biomass burning
227 plays a dominant role in the plumes of high CO (Fig. 2g-i). South American biomass burning leads to CO
228 enhancements between T14 and T16 of the Punta Arenas to Ascension flight. In the later portion of that
229 flight, biomass burning from Africa leads to strong CO plumes. Strong plumes of African biomass burning
230 are also seen at the beginning of the Ascension to Azores flight. GEOS-5 shows a strong plume around 800
231 hPa for the first hour of the flight, which agrees well with observations (Fig. 2b,d). The observations show
232 additional strong plumes in the next hour between 600 and 700 hPa. These plumes are present but
233 underestimated in GEOS-5, possibly due to errors in the magnitude of the emissions or the placement or
234 extent of the plumes. The placement and strength of simulated plumes is sensitive to the injection height of
235 the biomass burning, which is a source of uncertainty. In addition, plumes in models tend to dissipate more
236 quickly than in observations due to the numerical effects of limited model resolution (*Eastham and Jacob,*
237 2017).

238 The non-BB contribution to CO in the Atlantic reflects a mixture of global sources. Asian sources
239 make a notable contribution to the non-BB CO variability in the tropics (first half of the Ascension to Azores
240 flight), but as expected N. American sources become more dominant in the second half. In the northern
241 (later) portion of the Azores to Kangerlussuaq flight (Fig. 2), GEOS-5 attributes the observed plumes to
242 Eurasian biomass burning, but underestimates their magnitude. This flight also crosses the tropopause, and
243 both ATom-1 and GEOS-5 show a corresponding dip in CO concentrations. GEOS-5 predicts a plume of

244 enhanced CO due to N. American emissions around 11Z of the Azores to Kangerlussuaq flight that is not
245 seen in the observations (Fig. 2f,i). A similar error is made in the Kangerlussuaq to Minneapolis flight (Fig.
246 S5). This could be due to either an error in the assumed N. American sources, or to misplacement of the
247 plume by the model. A large overestimate of CO at the end of the Minneapolis to Palmdale flight also points
248 to a potential error in North American emissions from either fossil fuels or biomass burning.

249 **3.2 Model Evaluation Summary**

250 We summarize the comparison between the CO simulated by the GEOS-5 analyses and the QCLS
251 observations in Figure 3. The majority of points lie near the one-to-one line, indicating good overall
252 agreement between the GEOS-5 and observed CO distributions. The higher concentrations in the tropical
253 Atlantic compared to the tropical Pacific are evident in both the observations and model. Fig. 3 also reveals
254 occasional model overestimates of CO on flights over North America (green triangles), as well as
255 underestimates of high CO plumes over the North Pacific and Tropical Atlantic. An underestimate of
256 Eurasian biomass burning contributes to the model underestimates in the North Pacific and North Atlantic,
257 and has implications for ozone production in aged BB plumes [Liu *et al.*, in prep]. Globally, the correlation
258 of simulated and observed CO with 5-minute binning is $r=0.69$. Correlations for the Pacific, Atlantic, and
259 North America are 0.72, 0.80, and 0.80, respectively, while the correlation for the southern ocean is 0.053.
260 The poor correlation for the southern ocean reflects the very low variability of CO in this region. The model
261 performs far better at capturing the larger gradients present in the other regions. In general, the good
262 agreement between model outputs and observations testify the model forecasting skill and suggest the
263 suitability of using GEOS-5 forecast products to guide the design and execution of aircraft campaigns.

264 **4 Source Contributions to the Global CO Distribution**

265 **4.1 Global CO Distribution**

266 Figure 4 compares CO from GEOS-5 to the QCLS CO observations for the ATom-1 circuit including
267 the 11 total flight segments. The GEOS-5 CO is taken from the analysis closest to the mid-point of the flight
268 time and interpolated to the flight track following the longitude, latitude and pressure given in the
269 observations. We average both model CO and ATom measurements into one point per 360-seconds for easier
270 visualization.

271 Both model simulations and measurements show polluted air with higher CO mixing ratios in the
272 northern hemisphere than that in the southern hemisphere in August 2016. Over the northern hemispheric
273 polar region, the observations indicate highly polluted air with CO maxima occurring over Alaska and
274 northwest Canada, features also seen in the GEOS-5 simulation. Over the Atlantic section, CO maxima with
275 slightly lower values occur around the same latitude over west Greenland as shown both in observations and
276 model simulation. CO over the northern most locations along the ATom-1 circuit see some low values both
277 in model and observations, particularly north of 30°N and south of 40°S, due to the measurements occurring

278 in the stratosphere or occurring in the upper troposphere with stratospheric influence. Both model and
279 observations indicate that the air is relatively clean over the Pacific south of 30N with CO less than 70 ppb
280 and the CO minimum around 60S over the southeast Pacific. Over the Atlantic section, both model and
281 observations show low CO concentration south of 30S, but show a strong CO maximum over the tropical
282 Atlantic (5S-5N) with CO greater than 120 ppb. This high CO is mainly driven by southern hemisphere BB.
283 CO is slightly lower between 30N and 60N compared to that over tropical Atlantic and the Greenland. The
284 similarity between GEOS-5 and ATom-1 variability in neighboring points is due in part to the vertical
285 profiling which places horizontally extensive biomass burning layers in both model and presumably the
286 atmosphere at the same point along the track.

287 **4.2 CO Source Contributions**

288 We calculate the contribution of different CO sources to the total simulated CO using the GEOS-5
289 tagged CO tracers sampled along the ATom flight tracks. This analysis provides a picture of the dominant
290 sources affecting the constituent concentrations observed during ATom-1 for different regions of the
291 atmosphere. The tagging of CO sources includes both biomass burning (BB) and non-biomass burning (non-
292 BB) from four continental areas, with all other sources put into the “other” bin. Other BB sources are small,
293 but other non-BB sources are quite large as they include all natural sources as well as atmospheric
294 photochemical sources such as methane oxidation.

295 Figure 5 shows the contribution of each tagged tracer over the Pacific Ocean from 120°E to 110°W,
296 averaged over 5 degree latitude bins. Non-biomass burning sources dominate at all latitudes, due in part to
297 the inclusion of CO from methane oxidation in addition to fossil fuel sources in these tracers. The oxidation
298 of methane over the remote oceans contributes to the large magnitude of “other non-BB” sources over the
299 southern latitudes of the Pacific. Asian non-BB sources make the largest contribution to middle and upper
300 tropospheric CO (Fig. 5a) at the mid-latitudes of the North Pacific, with smaller contributions from N.
301 American and European non-BB sources. The largest biomass burning contribution comes from Africa in
302 the Southern Hemisphere and Tropics, switching to Eurasia in the northern latitudes.

303 Figure 5b shows the relative contributions in the lower troposphere, including the marine boundary
304 layer and defined here as pressures greater than 850 hPa. Missing bars indicate latitudes where no ATom-1
305 measurements were made in the lower troposphere. Asian non-BB CO makes a smaller contribution in the
306 lower troposphere than in the middle and upper troposphere. A strong CO maximum around 30°N is more
307 pronounced in the lower troposphere than above. This bin is not representative of the remote Pacific as it
308 includes Palmdale, California, with large contributions from local North American BB and non-BB sources.

309 The Atlantic flights (0°-60°W) show a large contribution from other non-BB sources in the Southern
310 Hemisphere with increasing contributions from Asian, N. American, and European non-BB CO as the flight
311 moves northward (Fig. 6), similar to the picture over the Pacific. However, the Atlantic receives a larger
312 contribution from biomass burning, particularly from Africa, over the Tropics. The contribution from African

313 BB is strong throughout the troposphere, but is particularly pronounced in the lower troposphere, where it
314 exceeds 100 ppb in the bins centered at 10°S and 5°N.

315 We also examine the tagged tracer contributions for each flight, including all altitudes sampled by
316 the flight (Fig. 7, Supp. Table S1). Flights occurring in the tropics and southern hemisphere (Flt. 1, 4-8)
317 receive 44-75% of the total CO from other non-BB sources. Other non-biomass burning sources include all
318 non-biomass burning sources located outside North America, Europe, and Asia. The contribution from
319 methane oxidation in addition to southern hemisphere emissions explains this large contribution. Flight 8
320 has a somewhat lower percent contribution from other non-BB sources than the other southern hemisphere
321 and tropical flights due to the higher percent contribution from African biomass burning. In contrast, the
322 Northern Hemisphere flights have a larger contribution from northern hemisphere source regions. Asian
323 non-BB explains over a third of the total CO for the northern Pacific flights (Flt. 2-3), while Asian and N.
324 American non-BB sources make comparable contributions to the North Atlantic and N. American flights (Flt.
325 9-11).

326 Since Figs. 5 and 6 reveal differences in source contributions between the lower troposphere and the
327 middle and upper troposphere, we also examine the source contributions to each flight for the lower
328 troposphere (Pressure > 850 hPa) only (Supp. Fig. S7). Asian sources make a larger percent contribution to
329 the Pacific flights (Flt. 0-4) when all flight altitudes are considered rather than the lower troposphere alone.
330 Regional sources such as African biomass burning for flights 6 and 7 and N. American sources for Flights 9
331 and 10 make a larger percent contribution in the lower troposphere.

332 **5 August 2016 in the Context of Interannual Variability (IAV)**

333 One of the major goals for the ATom campaign is to produce a climatology based on un-biased,
334 representative samples (Prather *et al.*, 2017). It is therefore important to consider whether August 2016 is a
335 “typical” boreal summer/austral winter month. Prather *et al.* [2018] found differences of 8-10% in the
336 chemical reactivity of model simulated air parcels when considering other years compared to 2016. We focus
337 here on the temporal representativeness of the ATom-1 campaign. Spatial representativeness is investigated
338 in Liu *et al.* [in prep]. August of 2016 was ENSO neutral, with a multivariate ENSO index (MEI) (Wolter
339 and Timlin, 1993); (<https://www.esrl.noaa.gov/psd/enso/mei>) of 0.175 for July/August. However, it was
340 preceded by strong El Nino conditions in 2015 and early 2016 (Blunden and Arndt, 2016). We therefore
341 consider whether the CO concentrations in August 2016 are typical or anomalous.

342 Multi-year satellite records provide a valuable tool for determining how CO concentrations in the
343 regions of the ATom-1 flights compare to previous years. We focus our analysis of CO interannual
344 variability on several regions traversed by the ATom flights. Figure 8 shows these regions in black squares
345 overplotted on the MOPITT CO column for August 2016. We also examine the IAV in BB sources from
346 nearby regions, outlined in red on Fig. 8. Figure 9 shows box-and-whisker plots of the mean, minimum, 25th,
347 50th, and 75th percentiles, and maximum in monthly mean August CO for each region over the 2000-2016
348 period for MOPITT (CO column and CO at 700 hPa) and 2004-2016 for MLS (CO at 215 hPa). The

349 corresponding time series are shown in Fig. 10. The variability in CO BB emissions from the Global Fire
350 Emissions Database version 4 (GFEDv4) (*van der Werf et al.*, 2017) for 2000-2016 is also shown for BB
351 regions that may affect the ATom flights. The BB emissions are averaged over June through August to
352 account for the persistence of CO in the atmosphere.

353 Among the regions mapped here, the tropical Atlantic shows the highest average CO values, as well
354 as the highest 2016 CO values, in both MOPITT and MLS observations (Fig. 9). This is consistent with large
355 biomass burning emissions from southern hemisphere (SH) Africa transported into the tropical Atlantic.
356 While SH Africa has the largest magnitude of biomass burning, its relative variability (variability relative to
357 the mean) is smaller than for the other regions (Fig. 9b). Similarly, the IAV in the MOPITT CO column and
358 700 hPa level over tropical Atlantic is smaller than that of the North Atlantic and Alaska regions. Although
359 the variability of CO over tropical Atlantic is relatively small, the MOPITT CO column shows a statistically
360 significant anti-correlation between the MOPITT CO column over the tropical Atlantic and the MEI ($r=-$
361 0.52). This relationship is not significant for the MOPITT 700 hPa level.

362 The time series of August MOPITT CO columns for both the North Atlantic and Alaska, regions
363 that show high variability, show a small but significant temporal correlation with summertime Siberian
364 biomass burning ($r=0.52$ for the North Atlantic and $r=0.59$ for Alaska). Slightly lower values are seen for
365 the 700 hPa MOPITT level. The time series of August MOPITT 700 hPa CO shows an increase in 2003 for
366 the North Atlantic and in 2002 and 2003 for Alaska (Fig. 10b,c). Previous studies attribute peaks in these
367 years to the presence of large forest fires in western Russia and Siberia, respectively (*Edwards et al.*,
368 2004; *Yashiro et al.*, 2009; *van der Werf et al.*, 2006). MOPITT CO values were below average in 2016 for
369 both the North Atlantic and Alaska even though Siberian biomass burning was above average in 2016 (Fig.
370 9a, b).

371 Since ENSO is known to drive large biomass burning variability in Indonesia (*van der Werf et al.*,
372 2006), we consider whether it may influence CO concentrations over the New Zealand region. Although the
373 MOPITT CO column over the Indonesia region does correlate with the MEI ($r=0.64$), there is no significant
374 correlation between June-Aug biomass burning in Indonesia and MOPITT CO over New Zealand. However,
375 August is not the peak season for Indonesian biomass burning (*Duncan et al.*, 2003b). The large Indonesian
376 fires that occurred during the strong 1997/1998 El Nino peaked during September to November (*Duncan et al.*,
377 2003a) and active fire detections for the 2015 Indonesian fires peaked in September and October (*Field*
378 *et al.*, 2016). Thus we might expect Indonesian biomass burning variability to have a greater influence on
379 CO variability during the September-October season, which was sampled in ATom-3.

380 How does 2016 compare to previous years? The MOPITT CO column shows tropical Atlantic CO
381 was near the 75th percentile, while the 700 hPa MOPITT level shows it close to the median. This difference
382 arises because the MOPITT column also includes information from the upper troposphere, and the MOPITT
383 200 hPa level (not shown) suggests CO levels for 2016 were near the 75th percentile. In contrast, MLS shows
384 that 2016 CO in the upper troposphere was much lower than average, near the 25th percentile. The MOPITT
385 v6 TIR product has a small positive bias drift in the upper troposphere of 0.78 % yr⁻¹ for the 200 hPa level

386 (*Deeter et al.*, 2014), which may contribute to the higher rank of 2016 in the MOPITT upper tropospheric
387 data compared to MLS. It is therefore hard to argue that 2016 was outside of the normal IAV for this region.

388 2016 CO in the North Atlantic and Alaska regions was below average in both the MOPITT column
389 and the 700 hPa level, and is in fact the lowest August value in the MOPITT record for the 700 hPa level
390 over Alaska. MLS also shows moderately low CO in the upper troposphere over Alaska in Aug. 2016.
391 Combined, this data suggests that the ATom-1 CO is not typical for the region. August 2016 CO column
392 values are also below the median over New Zealand and the eastern and central tropical Pacific, but the
393 relatively low variability of these regions makes this less of a concern for the representativeness of the ATom
394 measurements. The IAV of these regions is larger for the MOPITT 700 hPa level, and 2016 lies slightly
395 below the 25th percentile for this level.

396 The regionally-averaged 500 nm AOT from MODIS (Fig. 11) shows similar features to the MOPITT
397 column. The highest values are found for the tropical Atlantic, followed by the Alaska and North Atlantic
398 regions. This similarity is consistent with the importance of biomass burning emissions for both CO and
399 aerosols. However, the difference between the tropical Atlantic and the other regions is larger in the aerosol
400 case, while the difference between the North Atlantic and the Pacific regions is smaller. There is also greater
401 relative year-to-year variability over the tropical Atlantic for the aerosols than for CO. The shorter lifetime
402 of aerosols compared to CO, as well as the large contribution from biomass burning, likely explains the
403 greater prominence of the tropical Atlantic in the aerosol case. Furthermore, AOD (Fig. 12) shows a clear
404 peak in 2009 in several of the regions, whereas MOPITT data is missing for Aug. 2009, but MLS shows a
405 minimum (Tropical Atlantic) or no anomaly (other regions).

406 In summary, the multi-year satellite record shows considerable variability in CO, particularly over the
407 North Atlantic and Alaska. Concentrations during August 2016 were on the low end of the distribution for
408 most regions, especially in the lower troposphere. *Worden et al.* (2013) showed negative trends in the
409 MOPITT CO column significant at the one-sigma level for both the Northern and Southern hemispheres for
410 2000-2012. In addition, *Deeter et al.* (2014) report a small negative bias drift in the MOPITT V6 TIR product
411 in the lower troposphere, although drift in the column is almost negligible. Decreasing MOPITT CO over
412 time is also visible in some regions in Fig. 10. This negative trend may be contributing to the low values in
413 2016, although there is also substantial IAV in CO. Overall, the year 2016 shows anomalies for some regions,
414 but does not appear to be an extreme year.

415 **6 Conclusions**

416 We place the observations from the ATom-1 campaign in the context of interannual variability and
417 global source distributions using satellite observations and tagged tracers from GEOS-5, respectively.
418 GEOS-5 gives a reasonable reproduction of the background CO levels for most flights despite the use of
419 climatological fossil fuel and biofuel emissions, and captures the global distribution of CO observed during
420 ATom-1. Simulations with both forecast and analysis winds capture the timing of many of the enhanced CO
421 plumes encountered during the flights, although the magnitude of the enhancements was often

422 underestimated, which is not unexpected given the difference in resolution between the observations and
423 model. The strong performance of GEOS-5 with regards to the overall CO distribution and the timing of the
424 enhancements gives us confidence in using tagged tracers to identify the sources affecting the air sampled in
425 ATom-1.

426 We find that for most flights the dominant contribution to total CO is from non-biomass burning
427 sources, which include both fossil fuels and biofuels and oxidation of hydrocarbons including methane. An
428 exception to this is in the lower troposphere of the tropical Atlantic, where biomass burning from Africa
429 makes the largest contribution, exceeding 100 ppb in some locations. The non-BB source includes a large
430 fraction from Asia for flights over the North Pacific and from both Asia and North America for the North
431 Atlantic and North American flights, while other regions dominate in the Southern Hemisphere. Plumes of
432 elevated CO from both biomass burning and non-BB sources led to observations of enhanced CO during
433 ATom-1.

434 We use satellite observations of CO from MOPITT and MLS and AOT from MODIS to assess whether
435 August 2016, the period sampled by ATom-1, is typical or atypical in the context of IAV in the satellite
436 record (2000-2016). MOPITT and MLS show that CO in the lower and upper troposphere, respectively,
437 were below average in August 2016 compared to the satellite record for August for most of the regions
438 sampled by ATom-1, but not usually the minimum year. CO concentrations in the North Atlantic and Alaskan
439 regions show a positive correlation with Siberian biomass burning and large interannual variability. In
440 contrast, both MODIS AOT and the MOPITT CO column show above average values for the Tropical
441 Atlantic in 2016. This suggests that the high values of CO and aerosols from biomass burning encountered
442 during the tropical Atlantic portions of ATom may have been especially pronounced during this particular
443 year.

444 The seasonality of biomass burning, the OH distribution, and atmospheric transport pathways can alter
445 the source contributions from season to season. Thus, the next three ATom campaigns, which occur in
446 different seasons, will likely show variations in the relative source contributions to each region.

447

448 **Data Availability**

449 The QCLS data version used in this paper and the corresponding tagged-CO model output will be available
450 from the ORNL DAAC at <https://doi.org/10.3334/ORNLDAAC/1604>. MOPITT data is available at
451 <https://eosweb.larc.nasa.gov/datapool>. MLS data is available from <https://mls.jpl.nasa.gov/>. MODIS aerosol
452 data are available from <https://ladsweb.modaps.eosdis.nasa.gov/api/v1/productGroupPage/name=aerosol>.

453

454 **Acknowledgements**

455 The authors thank the NASA GMAO for providing the GEOS-5 forecasts and analyses. We thank the NASA
456 Earth Venture Suborbital Program, ESPO, and the pilots, crew and support staff of the DC-8.

457

458

459 **References**

- 460 ATom Science Team (2017), Moffett Field, CA, NASA Ames Earth Science Project Office (ESPO),
461 Accessed at doi: 10.5067/Aircraft/ATom/TraceGas_Aerosol_Global_Distribution
- 462 Bian, H., Colarco, P., Chin, M., Chen, G., Rodriguez, J., Liang, Q., Blake, D., Chu, D., da Silva, A.,
463 Darmenov, A., Diskin, G., Fuelberg, H., Huey, G., Kondo, Y., Nielsen, J., Pan, X., and Wisthaler, A.: Source
464 attributions of pollution to the Western Arctic during the NASA ARCTAS field campaign, *Atmospheric
465 Chemistry and Physics*, 13, 4707-4721, 10.5194/acp-13-4707-2013, 2013.
- 466 e.d. Blunden, J., and D. S. Arndt: State of the Climate in 2015. In: *Bull. Amer. Meteor. Soc.*, 97(8), 2016.
- 467 Darmenov, A. and A. da Silva, The Quick Fire Emissions Dataset (QFED): Documentation of versions 2.1,
468 2.2 and 2.4. NASA/TM-2015-104606, Vol. 38, 2015.
- 469 Deeter, M., Martinez-Alonso, S., Edwards, D., Emmons, L., Gille, J., Worden, H., Sweeney, C., Pittman, J.,
470 Daube, B., and Wofsy, S.: The MOPITT Version 6 product: algorithm enhancements and validation,
471 *Atmospheric Measurement Techniques*, 7, 3623-3632, 10.5194/amt-7-3623-2014, 2014.
- 472 Duncan, B., Bey, I., Chin, M., Mickley, L., Fairlie, T., Martin, R., and Matsueda, H.: Indonesian wildfires of
473 1997: Impact on tropospheric chemistry, *Journal of Geophysical Research-Atmospheres*, 108,
474 10.1029/2002JD003195, 2003a.
- 475 Duncan, B. N., Martin, R. V., Staudt, A. C., Yevich, R., and Logan, J. A.: Interannual and seasonal variability
476 of biomass burning emissions constrained by satellite observations, *Journal of Geophysical Research-
477 Atmospheres*, 108, 10.1029/2002jd002378, 2003b.
- 478 Duncan, B. N., Logan, J. A., Bey, I., Megretskaia, I. A., Yantosca, R. M., Novelli, P. C., Jones, N. B., and
479 Rinsland, C. P.: Global budget of CO, 1988-1997: Source estimates and validation with a global model, *J.
480 Geophys. Res. Atmos.*, 112, 10.1029/2007JD008459, 2007.
- 481 Duncan, B. N., and Logan, J. A.: Model analysis of the factors regulating the trends and variability of carbon
482 monoxide between 1988 and 1997, *Atmospheric Chemistry and Physics*, 8, 7389-7403, 2008.
- 483 Eastham, S. D. and Jacob, D. J.: Limits on the ability of global Eulerian models to resolve intercontinental
484 transport of chemical plumes, *Atmos. Chem. Phys.*, 17, 2543-2553, doi:10.5194/acp-17-2543-2017, 2017.
- 485 Edwards, D., Petron, G., Novelli, P., Emmons, L., Gille, J., and Drummond, J.: Southern Hemisphere carbon
486 monoxide interannual variability observed by Terra/Measurement of Pollution in the Troposphere
487 (MOPITT), *Journal of Geophysical Research-Atmospheres*, 111, 10.1029/2006JD007079, 2006.
- 488 Edwards, D. P., Emmons, L. K., Hauglustaine, D. A., Chu, D. A., Gille, J. C., Kaufman, Y. J., Petron, G.,
489 Yurganov, L. N., Giglio, L., Deeter, M. N., Yudin, V., Ziskin, D. C., Warner, J., Lamarque, J. F., Francis, G.
490 L., Ho, S. P., Mao, D., Chen, J., Grechko, E. I., and Drummond, J. R.: Observations of carbon monoxide and
491 aerosols from the Terra satellite: Northern Hemisphere variability, *Journal of Geophysical Research-
492 Atmospheres*, 109, 10.1029/2004jd004727, 2004.
- 493 Emmons, L., Pfister, G., Edwards, D., Gille, J., Sachse, G., Blake, D., Wofsy, S., Gerbig, C., Matross, D.,
494 and Nedelec, P.: Measurements of Pollution in the Troposphere (MOPITT) validation exercises during

495 summer 2004 field campaigns over North America, *Journal of Geophysical Research-Atmospheres*, 112,
496 10.1029/2006JD007833, 2007.

497 Field, R., van der Werf, G., Fanin, T., Fetzer, E., Fuller, R., Jethva, H., Levy, R., Livesey, N., Luo, M., Torres,
498 O., and Worden, H.: Indonesian fire activity and smoke pollution in 2015 show persistent nonlinear
499 sensitivity to El Nino-induced drought, *Proceedings of the National Academy of Sciences of the United States*
500 *of America*, 113, 9204-9209, 10.1073/pnas.1524888113, 2016.

501 Heald, C., Jacob, D., Fiore, A., Emmons, L., Gille, J., Deeter, M., Warner, J., Edwards, D., Crawford, J.,
502 Hamlin, A., Sachse, G., Browell, E., Avery, M., Vay, S., Westberg, D., Blake, D., Singh, H., Sandholm, S.,
503 Talbot, R., and Fuelberg, H.: Asian outflow and trans-Pacific transport of carbon monoxide and ozone
504 pollution: An integrated satellite, aircraft, and model perspective, *Journal of Geophysical Research-*
505 *Atmospheres*, 108, 10.1029/2003JD003507, 2003.

506 Hsu, J., Prather, M., Wild, O., Sundet, J., Isaksen, I., Browell, E., Avery, M., and Sachse, G.: Are the TRACE-
507 P measurements representative of the western Pacific during March 2001?, *Journal of Geophysical Research-*
508 *Atmospheres*, 109, 10.1029/2003JD004002, 2004.

509 Kasischke, E., Hyer, E., Novelli, P., Bruhwiler, L., French, N., Sukhinin, A., Hewson, J., and Stocks, B.:
510 Influences of boreal fire emissions on Northern Hemisphere atmospheric carbon and carbon monoxide,
511 *Global Biogeochemical Cycles*, 19, 10.1029/2004GB002300, 2005.

512 Langenfelds, R., Francey, R., Pak, B., Steele, L., Lloyd, J., Trudinger, C., and Allison, C.: Interannual growth
513 rate variations of atmospheric CO₂ and its delta C-13, H-2, CH₄, and CO between 1992 and 1999 linked to
514 biomass burning, *Global Biogeochemical Cycles*, 16, 10.1029/2001GB001466, 2002.

515 Levy, R., Hsu, C., et al.: MODIS Atmosphere L2 Aerosol Product. NASA MODIS Adaptive Processing
516 System, Goddard Space Flight Center, USA, doi:http://dx.doi.org/10.5067/MODIS/MYD04_L2.006, 2015.

517 Liu, J., J. A. Logan, L. T. Murray, H. C. Pumphrey, and I. A. Megretskaja, Transport analysis and source
518 attribution of seasonal and interannual variability of CO in the tropical upper troposphere and lower
519 stratosphere. *Atmos. Chem. Phys.*, **13**: 129-146 doi:[10.5194/acp-13-129-2013](https://doi.org/10.5194/acp-13-129-2013), 2013.

520 Livesey, N., Filipiak, M., Froidevaux, L., Read, W., Lambert, A., Santee, M., Jiang, J., Pumphrey, H., Waters,
521 J., Cofield, R., Cuddy, D., Daffer, W., Drouin, B., Fuller, R., Jarnot, R., Jiang, Y., Knosp, B., Li, Q., Perun,
522 V., Schwartz, M., Snyder, W., Stek, P., Thurstans, R., Wagner, P., Avery, M., Browell, E., Cammas, J.,
523 Christensen, L., Diskin, G., Gao, R., Jost, H., Loewenstein, M., Lopez, J., Nedelec, P., Osterman, G., Sachse,
524 G., and Webster, C.: Validation of Aura Microwave Limb Sounder O-3 and CO observations in the upper
525 troposphere and lower stratosphere, *Journal of Geophysical Research-Atmospheres*, 113,
526 10.1029/2007JD008805, 2008.

527 Logan, J., Megretskaja, I., Nassar, R., Murray, L., Zhang, L., Bowman, K., Worden, H., and Luo, M.: Effects
528 of the 2006 El Nino on tropospheric composition as revealed by data from the Tropospheric Emission
529 Spectrometer (TES), *Geophysical Research Letters*, 35, 10.1029/2007GL031698, 2008.

530 Lucchesi, R, File Specification for GEOS-5 FP. GMAO Office Note No. 4 (Version 1.1), 61pp, 2017,
531 available from http://gmao.gsfc.nasa.gov/pubs/office_notes.

532 Molod, A., Takacs, L., Suarez, M., and Bacmeister, J.: Development of the GEOS-5 atmospheric general
533 circulation model: evolution from MERRA to MERRA2, *Geoscientific Model Development*, 8, 1339-1356,
534 10.5194/gmd-8-1339-2015, 2015.

535 Novelli, P., Masarie, K., Lang, P., Hall, B., Myers, R., and Elkins, J.: Reanalysis of tropospheric CO trends:
536 Effects of the 1997-1998 wildfires, *Journal of Geophysical Research-Atmospheres*, 108,
537 10.1029/2002JD003031, 2003.

538 Ott, L., Duncan, B., Pawson, S., Colarco, P., Chin, M., Randles, C., Diehl, T., and Nielsen, E.: Influence of
539 the 2006 Indonesian biomass burning aerosols on tropical dynamics studied with the GEOS-5 AGCM,
540 *Journal of Geophysical Research-Atmospheres*, 115, 10.1029/2009jd013181, 2010.

541 Pfister, G., Emmons, L., Edwards, D., Arellano, A., Sachse, G., and Campos, T.: Variability of springtime
542 transpacific pollution transport during 2000-2006: the INTEX-B mission in the context of previous years,
543 *Atmospheric Chemistry and Physics*, 10, 1345-1359, 10.5194/acp-10-1345-2010, 2010.

544 Prather, M., Zhu, X., Flynn, C., Strode, S., Rodriguez, J., Steenrod, S., Liu, J., Lamarque, J., Fiore, A.,
545 Horowitz, L., Mao, J., Murray, L., Shindell, D., and Wofsy, S.: Global atmospheric chemistry - which air
546 matters, *Atmospheric Chemistry and Physics*, 17, 9081-9102, 10.5194/acp-17-9081-2017, 2017.

547 Reinecker, M. M. et al., The GEOS-5 Data Assimilation System – Documentation of Versions 5.0.1, 5.1.0,
548 and 5.2.0, Technical Report Series on Global Modeling and Data Assimilation, Vol. 27, ed. M. J. Suarez,
549 NASA/TM-2008-104606, 2008.

550 Prather, M. J., Flynn, C. M., Zhu, X., Steenrod, S. D., Strode, S. A., Fiore, A. M., Correa, G., Murray, L. T.,
551 and Lamarque, J.-F.: How well can global chemistry models calculate the reactivity of short-lived greenhouse
552 gases in the remote troposphere, knowing the chemical composition, *Atmos. Meas. Tech.*, 11, 2653-2668,
553 <https://doi.org/10.5194/amt-11-2653-2018>, 2018.

554 Rienecker, M. M., Suarez, M. J., Gelaro, R., Todling, R., Bacmeister, J., Liu, E., Bosilovich, M. G., Schubert,
555 S. D., Takacs, L., Kim, G.-K., Bloom, S., Chen, J., Collins, D., Conaty, A., da Silva, A., Gu, W., Joiner, J.,
556 Koster, R. D., Lucchesi, R., Molod, A., Owens, T., Pawson, S., Pegion, P., Redder, C. R., Reichle, R.,
557 Robertson, F. R., Ruddick, A. G., Sienkiewicz, M., and Woollen, J.: MERRA: NASA's Modern-Era
558 Retrospective Analysis for Research and Applications, *Journal of Climate*, 24, 3624-3648, 10.1175/JCLI-D-
559 11-00015.1, 2011.

560 Santoni, G., Daube, B., Kort, E., Jimenez, R., Park, S., Pittman, J., Gottlieb, E., Xiang, B., Zahniser, M.,
561 Nelson, D., McManus, J., Peischl, J., Ryerson, T., Holloway, J., Andrews, A., Sweeney, C., Hall, B., Hints, A.,
562 Moore, F., Elkins, J., Hurst, D., Stephens, B., Bent, J., and Wofsy, S.: Evaluation of the airborne quantum
563 cascade laser spectrometer (QCLS) measurements of the carbon and greenhouse gas suite - CO₂, CH₄, N₂O,
564 and CO - during the CalNex and HIPPO campaigns, *Atmospheric Measurement Techniques*, 7, 1509-1526,
565 10.5194/amt-7-1509-2014, 2014.

566 Strode, S. A., and Pawson, S.: Detection of carbon monoxide trends in the presence of interannual variability,
567 *Journal of Geophysical Research-Atmospheres*, 118, 12257-12273, 10.1002/2013JD020258, 2013.

568 van der Werf, G., Randerson, J., Giglio, L., Collatz, G., Kasibhatla, P., and Arellano, A.: Interannual
569 variability in global biomass burning emissions from 1997 to 2004, *Atmospheric Chemistry and Physics*, 6,
570 3423-3441, 2006.

571 van der Werf, G. R., Randerson, J. T., Giglio, L., van Leeuwen, T. T., Chen, Y., Rogers, B. M., Mu, M., van
572 Marle, M. J. E., Morton, D. C., Collatz, G. J., Yokelson, R. J., and Kasibhatla, P. S.: Global fire emissions
573 estimates during 1997–2016, *Earth Syst. Sci. Data*, 9, 697-720, <https://doi.org/10.5194/essd-9-697-2017>,
574 2017.

575 Voulgarakis, A., Marlier, M., Faluvegi, G., Shindell, D., Tsigaridis, K., and Mangeon, S.: Interannual
576 variability of tropospheric trace gases and aerosols: The role of biomass burning emissions, *Journal of*
577 *Geophysical Research-Atmospheres*, 120, 7157-7173, 10.1002/2014JD022926, 2015.

578 Waters, J., Froidevaux, L., Harwood, R., Jarnot, R., Pickett, H., Read, W., Siegel, P., Cofield, R., Filipiak,
579 M., Flower, D., Holden, J., Lau, G., Livesey, N., Manney, G., Pumphrey, H., Santee, M., Wu, D., Cuddy, D.,
580 Lay, R., Loo, M., Perun, V., Schwartz, M., Stek, P., Thurstans, R., Boyles, M., Chandra, K., Chavez, M.,
581 Chen, G., Chudasama, B., Dodge, R., Fuller, R., Girard, M., Jiang, J., Jiang, Y., Knosp, B., LaBelle, R., Lam,
582 J., Lee, K., Miller, D., Oswald, J., Patel, N., Pukala, D., Quintero, O., Scaff, D., Van Snyder, W., Tope, M.,
583 Wagner, P., and Walch, M.: The Earth Observing System Microwave Limb Sounder (EOS MLS) on the Aura
584 satellite, *Ieee Transactions on Geoscience and Remote Sensing*, 44, 1075-1092,
585 10.1109/TGRS.2006.873771, 2006.

586 Wolter, K., and Timlin, M. S.: Monitoring ENSO in COADS with a seasonally adjusted principal component
587 index, *Proc. of the 17th Climate Diagnostics Workshop*, 1993,

588 Worden, H. M., Deeter, M. N., Frankenberg, C., George, M., Nichituu, F., Worden, J., Aben, I., Bowman, K.
589 W., Clerbaux, C., Coheur, P. F., de Laat, A. T. J., Detweiler, R., Drummond, J. R., Edwards, D. P., Gille, J.
590 C., Hurtmans, D., Luo, M., Martinez-Alonso, S., Massie, S., Pfister, G., and Warner, J. X.: Decadal record
591 of satellite carbon monoxide observations, *Atmospheric Chemistry and Physics*, 13, 837-850, 10.5194/acp-
592 13-837-2013, 2013.

593 Yashiro, H., Sugawara, S., Sudo, K., Aoki, S., and Nakazawa, T.: Temporal and spatial variations of carbon
594 monoxide over the western part of the Pacific Ocean, *Journal of Geophysical Research-Atmospheres*, 114,
595 10.1029/2008JD010876, 2009.

596 Ziemke, J., and Chandra, S.: La Nina and El Nino-induced variabilities of ozone in the tropical lower
597 atmosphere during 1970-2001, *Geophysical Research Letters*, 30, 10.1029/2002GL016387, 2003.

598

599 **Table 1 : Regional August 2016 CO Emission Totals in the GEOS-5 FP Simulations**

	Fossil Fuel¹	Biogenic¹	BB¹
North America	6.7 (8.0)	5.8	2.4 (2.7)
Europe	4.9 (5.9)	2.4	
Asia	26 (31)	7.9	
Eurasia ²			3.0 (3.3)
Africa			24 (27)
South America	13 (16)	17	11 (12)
Other ³			2.9 (3.2)
Global	50 (60)	34	43 (48)

600 ¹Emissions are in units of Tg. Values in parentheses include the 20% and 11% scaling factors for fossil fuels
 601 and biomass burning, respectively, to account for CO production from VOC oxidation.

602 ²The Eurasian tagged tracer for BB CO includes emissions from Europe and northern Asia, but excludes
 603 southern Asia.

604 ³Other fossil fuel emissions includes emissions from Africa and South America, while other BB emissions
 605 excludes those regions since they are tagged separately. Other BB does include southern Asia as well
 606 Australia.

607

608 **Table 2: Mean and Standard Deviations in CO along Atlantic and Pacific Flight Tracks**

Region	Flight	Obs Mean (ppb)	Obs Stdev (ppb)	Model Mean (ppb)	Model Stdev (ppb)
Eastern Pacific	1. Palmdale – Palmdale	75	14	77	19
	2. Palmdale - Anchorage	100	40	88	16
Pacific	3. Anchorage-Kona	85	36	81	18
	4. Kona –Pago Pago	61	5.1	63	5.5
	5. Pago Pago – Christchurch	55	11	57	6.1
Southern Ocean	6. Christchurch – Punta Arenas	56	6.4	54	4.7
Atlantic	7. Punta Arenas – Ascension	69	17	71	26
	8. Ascension – Azores	101	36	103	27

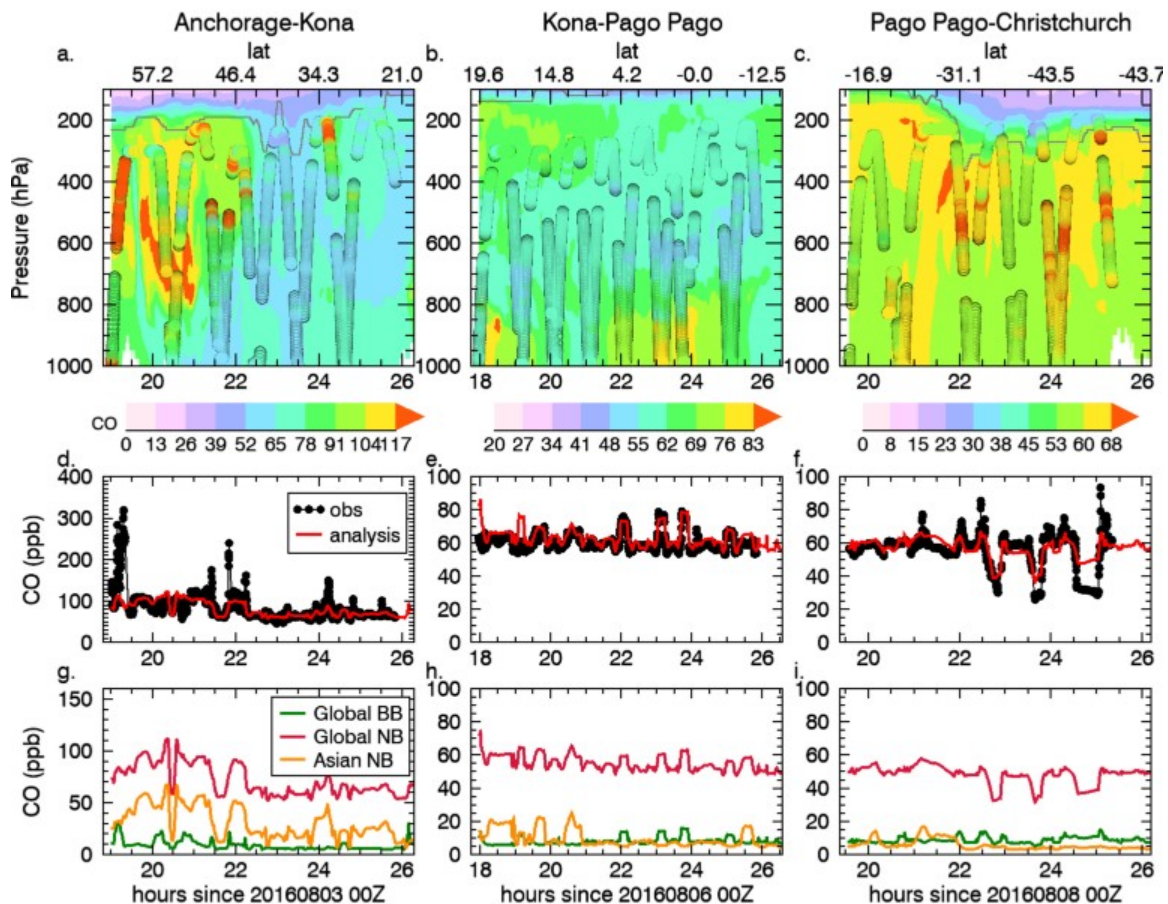
	9. Azores – Kangerlussuaq	88	32	87	19
N. America	10. Kangerlussuaq – Minneapolis	90	26	91	22
	11. Minneapolis – Palmdale	84	38	107	78

609

610

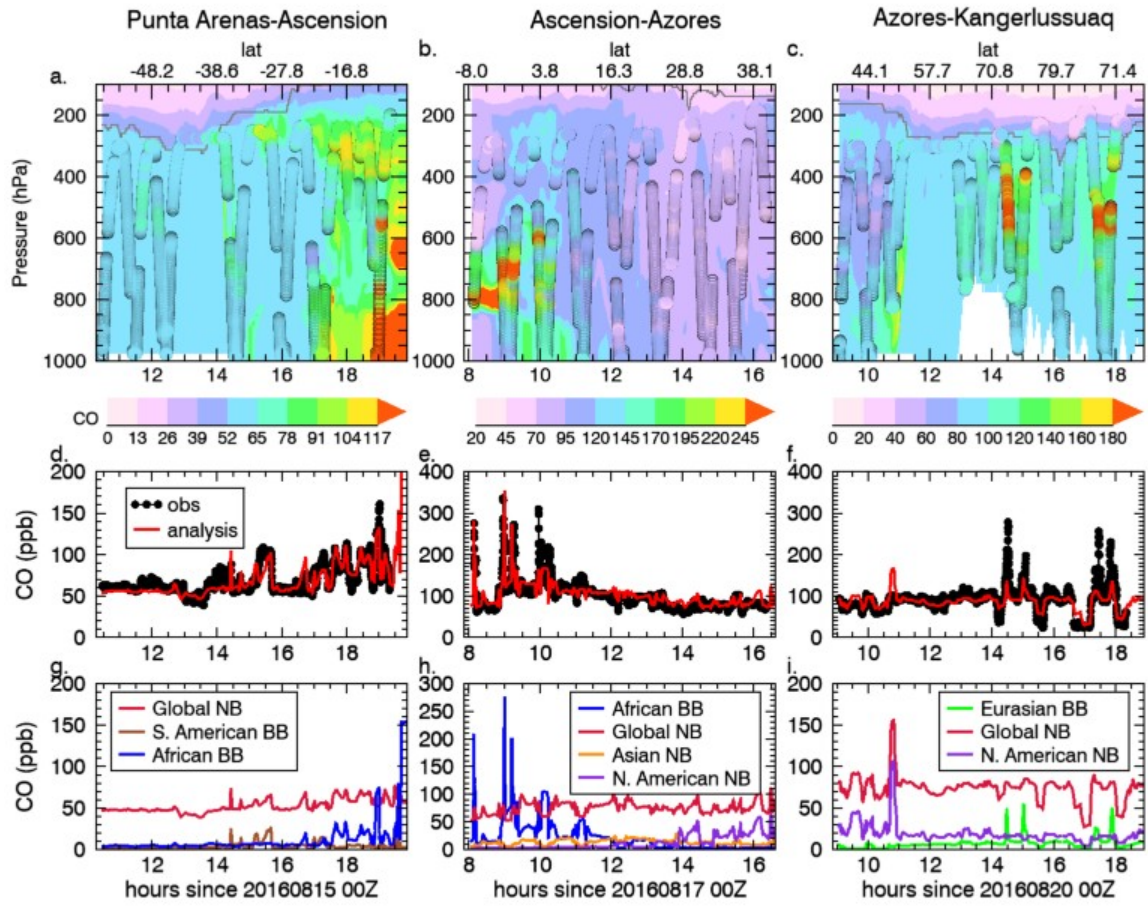
611

612



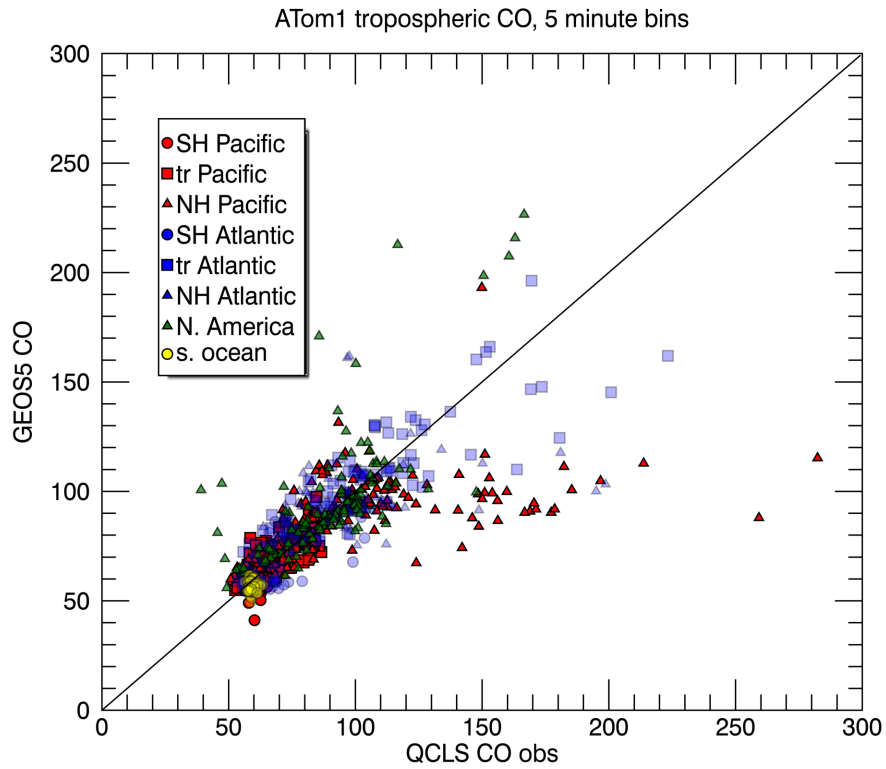
613

614 **Figure 1: Curtain plot of CO (ppb) from the GEOS-5 analysis as a function of time and pressure overplotted with**
615 **the model tropopause (gray line) and QCLS CO observations (circles) (top row) for the a) Anchorage to Kona**
616 **flight, b) Kona to Pago Pago flight, and c) Pago Pago to Christchurch flight. Axis ranges vary between panels due**
617 **to the large range of concentrations encountered. The top x-axis indicates the latitudes of the flight track. d-f)**
618 **The GEOS-5 CO interpolated to the flight track (red line) is compared to the observations (black circles). g-h)**
619 **Tagged tracer contributions to the GEOS-5 CO.**



620

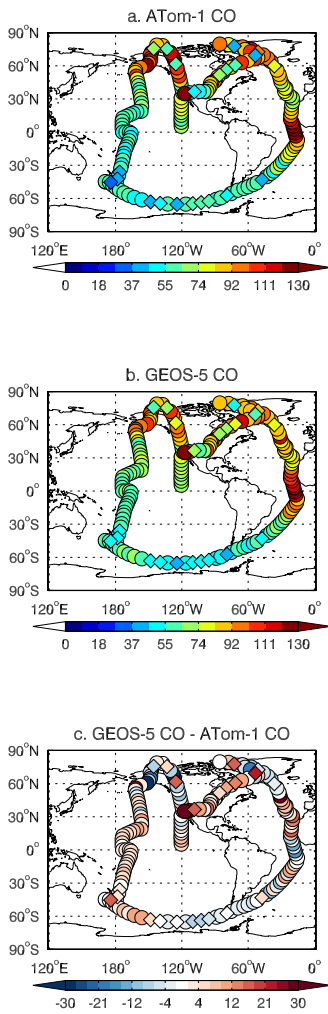
621 Figure 2: As in Fig. 1, but for the Atlantic flights: a,d,g) Punta Arenas-Ascension Island, b,e,h) Ascension Island
 622 to the Azores, and c,f,i) Azores to Kangerlussuaq.



623

624 **Figure 3: GEOS-5 simulated CO versus QCLS CO observations for all ATom-1 flights averaged into 5 minute**
 625 **bins. CO is in units of ppb. Pacific flights are shown in red, Atlantic flights in blue, N. American flights in green,**
 626 **and southern ocean flights in yellow. Circles indicate Southern Hemisphere points, triangles indicate Northern**
 627 **Hemisphere points, and squares indicate tropical points. The one-to-one line is overplotted in black.**

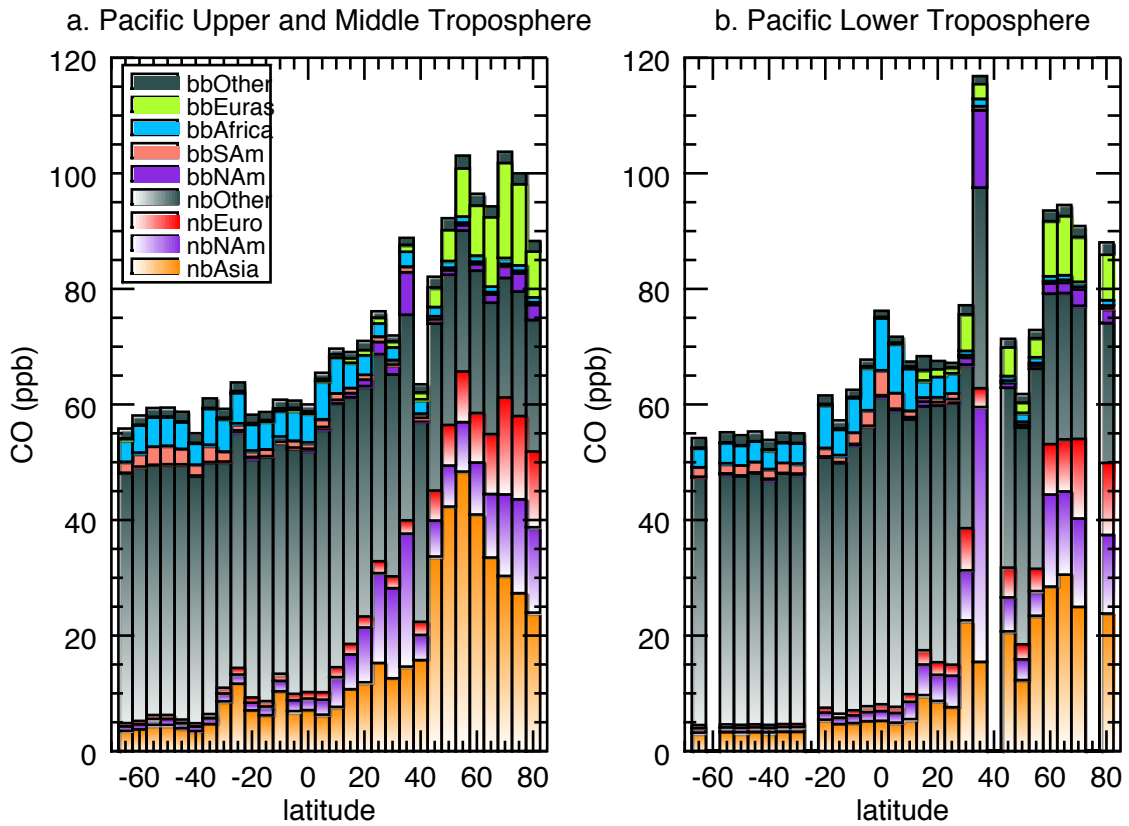
628



629

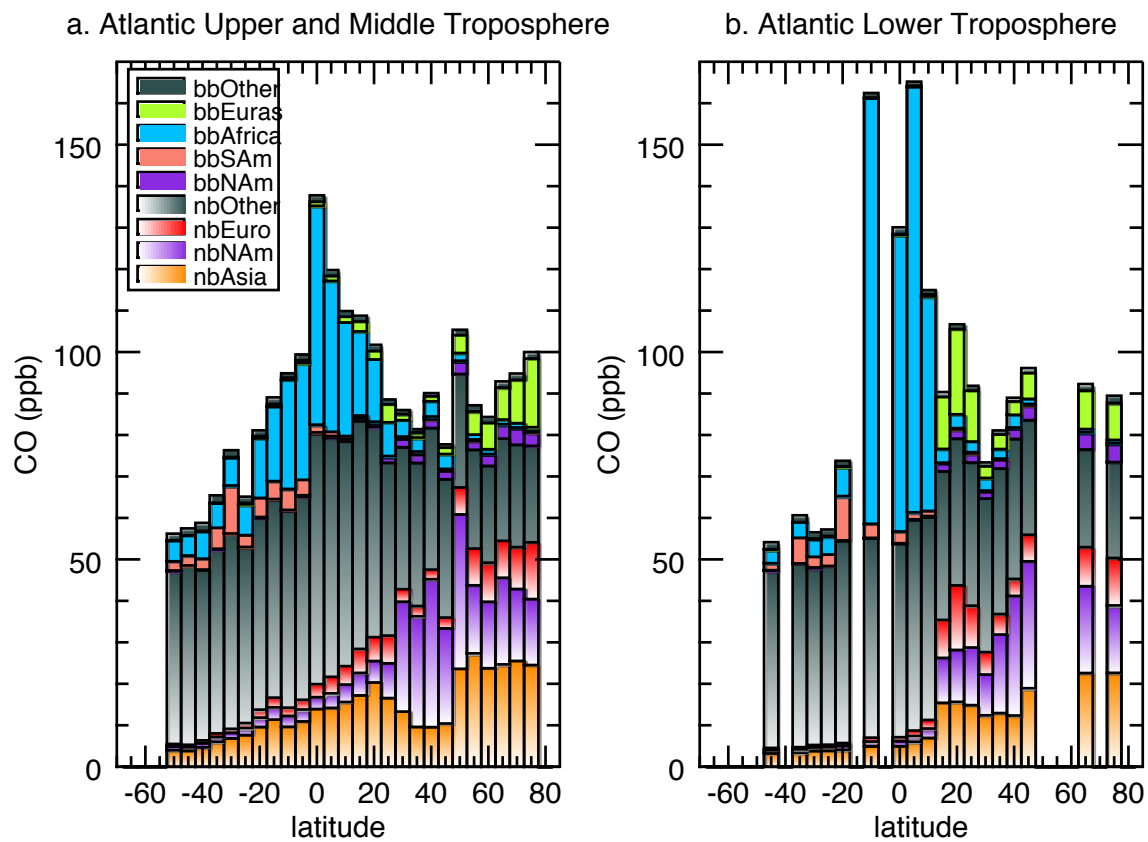
630 **Figure 4: CO (ppb) from the (a) QCLS observations, (b) GEOS-5 analysis, and (c) the GEOS-5 – obs difference**
 631 **for the ATom-1 circuit including all 11 research flight segments. The GEOS-5 CO is taken from the analysis**
 632 **closest to the mid-point of the flight time and interpolated to the flight track following the longitude, latitude and**
 633 **pressure given in the observations. Both model forecast and ATom measurements are averaged into a sample rate**
 634 **of one per 360-second. Data in the troposphere are plotted in a circle, while data in the stratosphere are plotted in**
 635 **a diamond, based on the GEOS-5 tropopause.**

636



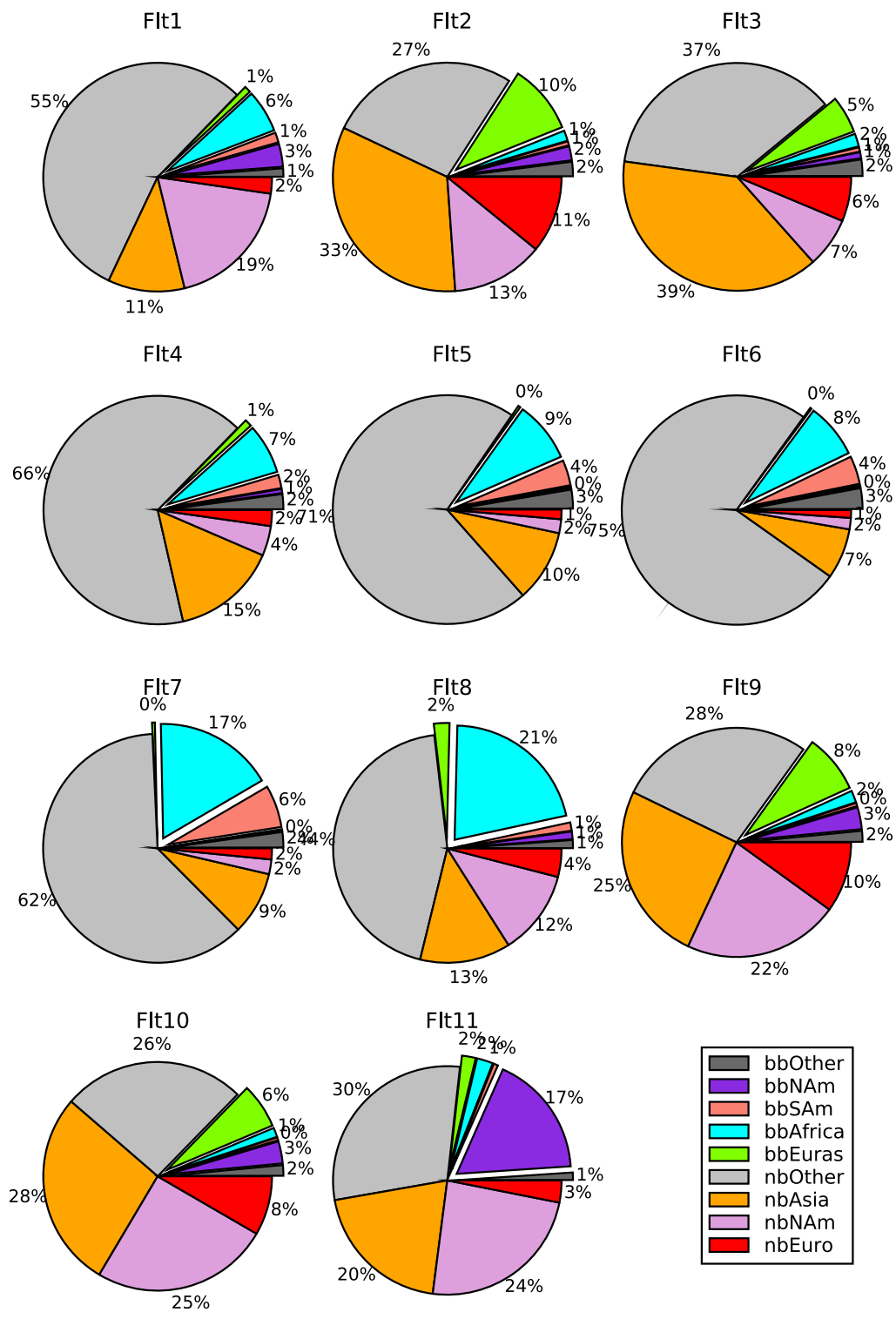
637

638 **Figure 5: The contribution of each tagged CO tracer over the Pacific in the (a) upper and middle troposphere**
 639 **(pressure ≤ 850 hPa) and (b) lower troposphere (pressure > 850 hPa). Data from multiple flights over the region**
 640 **between 120°E and 110°W is included, with each bar representing data averaged over a 5 degree latitude bin.**
 641 **Shaded bars represent non-BB CO from Asia (orange), N. America (purple), Europe (red), and the rest of the**
 642 **world (gray). Solid bars represent BB CO from N. America (purple), S. America (pink), Africa (cyan), Eurasia**
 643 **(green), and the rest of the world (gray).**



644

645 **Figure 6: As in Fig. 5, but for the Atlantic. Data from multiple flights over the region 0-60°W is included, with**
 646 **each bar representing data averaged over a 5 degree latitude bin.**

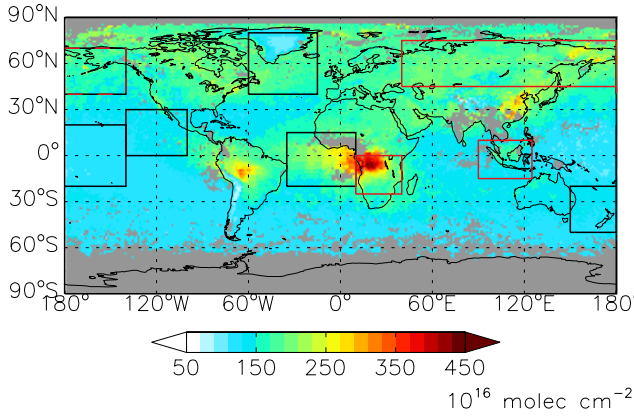


647

648 **Figure 7: Percent contributions of tagged tracers to total CO for each flight. Exploded slices represent the biomass**
 649 **burning tracers: North American (purple), S. American (salmon), African (cyan), Eurasian (green), and Other**

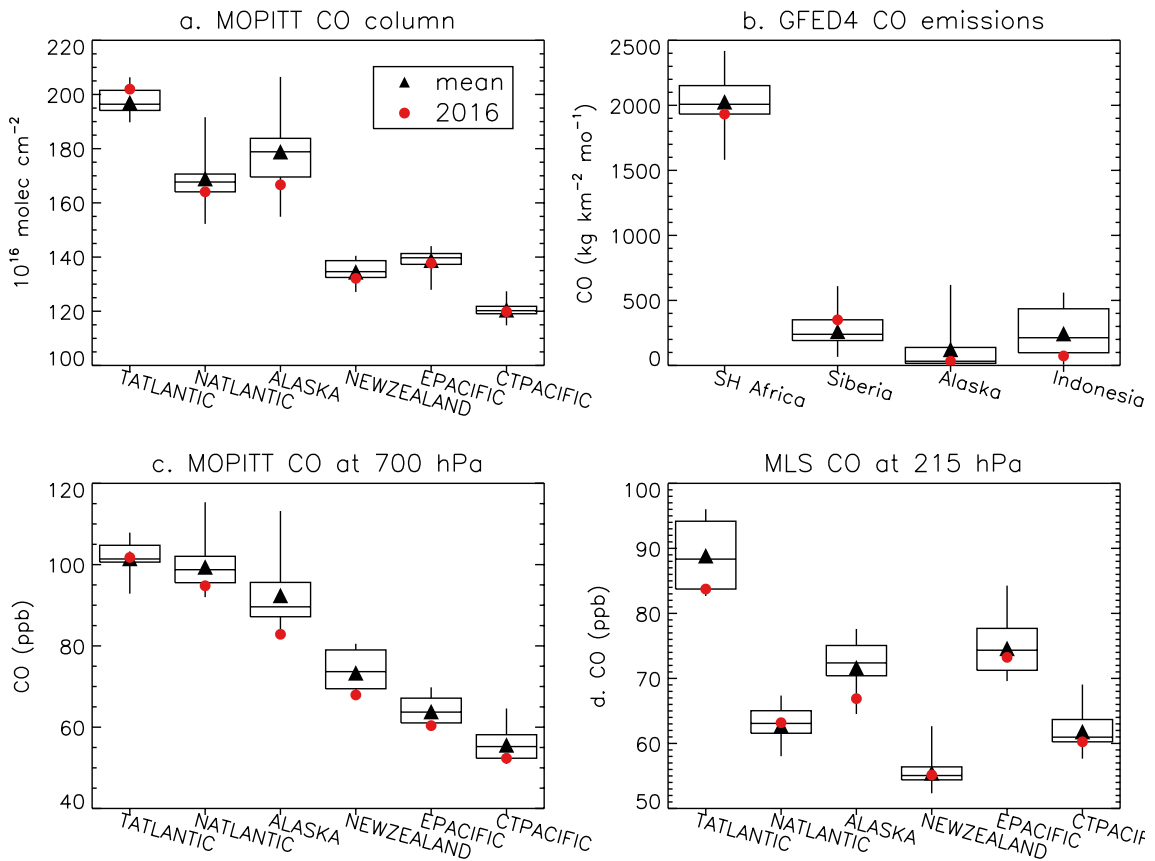
650 (dark gray). The non-biomass burning (nb) tracers are for Asia (orange), N. America (lavender), Europe (red),
 651 and other (light gray).

652



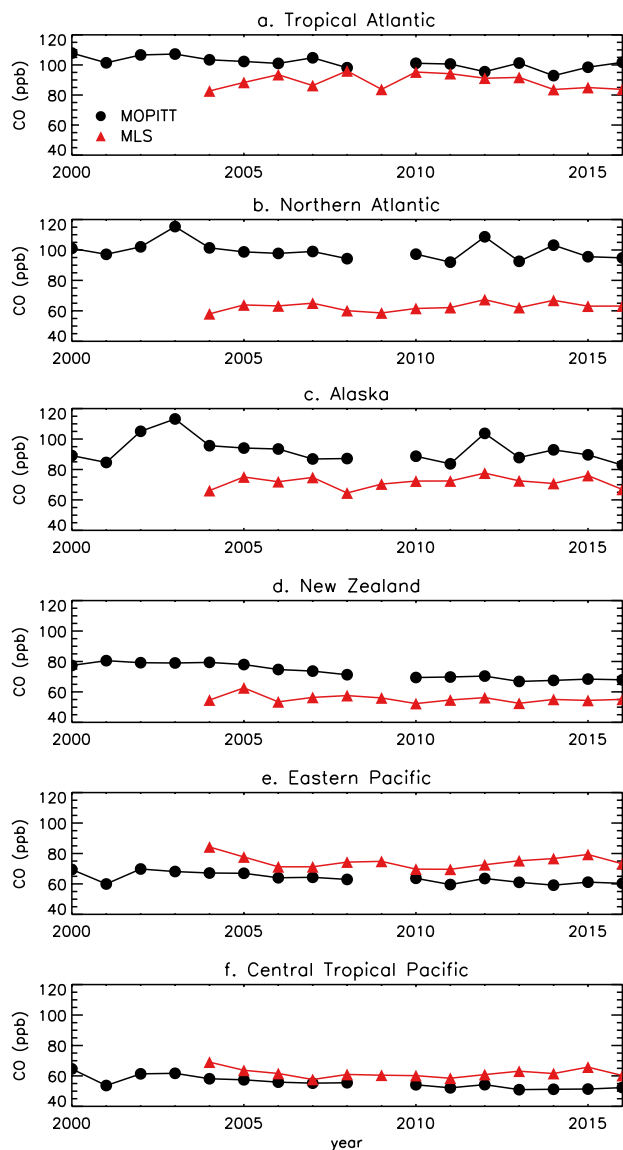
653

654 **Figure 8: MOPITT CO column for August 2016 overplotted with the regions shown in Fig. 10. Black rectangles**
 655 **indicate the regions where we analyze CO concentrations, and red rectangles indicate the regions used for biomass**
 656 **burning.**



657

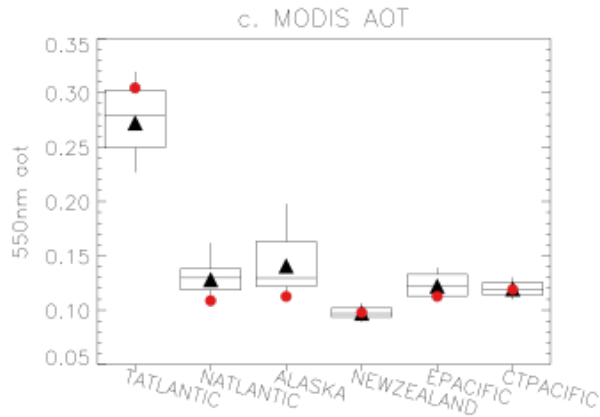
658 **Figure 9: Boxes show the 25th, 50th, and 75th percentile values; whiskers show the minimum and maximum values;**
 659 **black triangles show the mean value, and red circles show the 2016 value for a) the MOPITT CO column, b) the**
 660 **GFED4 CO emissions, c) MOPITT CO at 700 hPa, and d) MLS CO at 215 hPa. Statistics for MOPITT are for**
 661 **2000-2016, statistics for GFED4 are for 2000-2015, and statistics for MLS are for 2004-2016. MOPITT and MLS**
 662 **values are for August, while the GFED4 emissions are averaged over June through August.**



663

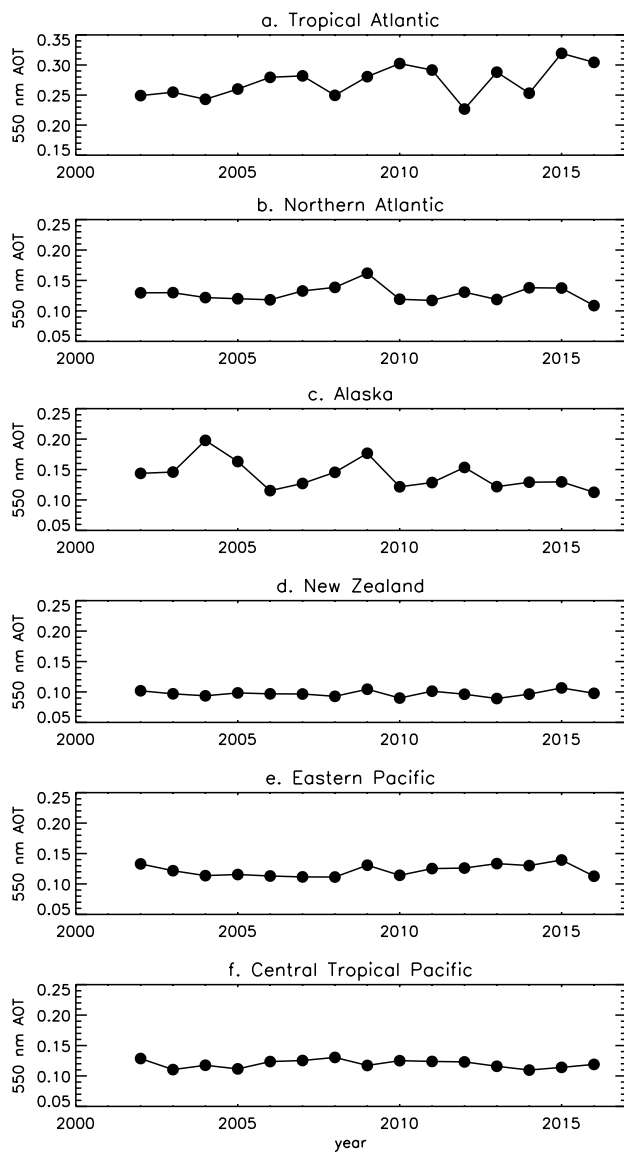
664

665 **Figure 10: Time series of August MOPITT CO at the 700 hPa level (black circles) and MLS CO (red triangles)**
 666 **at the 215 hPa level for the 6 regions shown in black in Fig. 8.**



667

668 **Figure 11: As in Figure 9, but for the August MODIS 550 nm AOT. Only values over oceans are included in the**
 669 **regional averages.**



670
671

Figure 12: Time series of regionally averaged August MODIS 550 nm AOT. Only values over oceans are included

672 in the regional averages. The y-axis range for panel a differs from the other panels due to the higher AOT values
673 in that region.

